Front. Mech. Eng. 2018, 13(1): 53–65
https://doi.org/10.1007/s11465-017-0437-y

RESEARCH ARTICLE

M. WU, M. AHMADEIN, A. LUDWIG

Premature melt solidification during mold filling and its influence on the as-cast structure

Abstract Premature melt solidification is the solidification of a melt during mold filling. In this study, a numerical model is used to analyze the influence of the pouring process on the premature solidification. The numerical model considers three phases, namely, air, melt, and equiaxed crystals. The crystals are assumed to have originated from the heterogeneous nucleation in the undercooled melt resulting from the first contact of the melt with the cold mold during pouring. The transport of the crystals by the melt flow, in accordance with the so-called "big bang" theory, is considered. The crystals are assumed globular in morphology and capable of growing according to the local constitutional undercooling. These crystals can also be remelted by mixing with the superheated melt. As the modeling results, the evolutionary trends of the number density of the crystals and the volume fraction of the solid crystals in the melt during pouring are presented. The calculated number density of the crystals and the volume fraction of the solid crystals in the melt at the end of pouring are used as the initial conditions for the subsequent solidification simulation of the evolution of the as-cast structure. A five-phase volume-average model for mixed columnar-equiaxed solidification is used for the solidification simulation. An improved agreement between the simulation and experimental results is achieved by considering the effect of premature melt solidification during mold filling. Finally, the influences of pouring parameters, namely, pouring temperature, initial mold temperature, and pouring rate, on the premature melt solidification are discussed.

Keywords premature solidification, mold filling, as-cast structure, modeling

Received December 2, 2016; accepted January 10, 2017

M. WU (✉), A. LUDWIG
Chair for Simulation and Modeling of Metallurgical Processes, University of Leoben, Leoben A-8700, Austria
E-mail: menghuai.wu@unileoben.ac.at

M. WU
Christian-Doppler Laboratory for Advanced Process Simulation of Solidification and Melting, Department of Metallurgy, University of Leoben, Leoben A-8700, Austria

M. AHMADEIN
Production Engineering and Mechanical Design Department, Faculty of Engineering, Tanta University, Tanta 31111, Egypt

1 Introduction

The typical as-cast structure of gravity castings or ingots consists of equiaxed and/or columnar crystal zones. Primary theories describing the formation of these crystal zones focus highly on the origin of equiaxed crystals [1,2]. A casting that is poured with superheated melt without sufficient equiaxed inoculants develops a dominant columnar structure, whereas a casting that is well inoculated and poured with less superheated melt can develop a complete equiaxed structure. Several plausible formation mechanisms of equiaxed crystals in engineering castings have been proposed. The first is the heterogeneous nucleation in the bulk melt when it becomes constitutionally undercooled [3]. The second is the "big-bang" theory, which posits that the crystals originate from the undercooled melt at the mold wall during pouring; some of these crystals survive at low superheat, and they are transported by the melt flow to the inner region of the casting [4]. The third is the fragmentation of columnar dendrites because of the local remelting induced by flow and temperature fluctuation, and the crystal fragments are transported to the bulk melt region [5]. The fourth proposed mechanism is "crystal showering," or crystal settling, which occurs on the top free surface of the casting; the melt is undercooled, and nucleation occurs on this surface [6]. Unlike the first mechanism, which involves the constitutional undercooling of the bulk melt, the other three mechanisms all suggest that the transport of the crystal nuclei by the melt flow plays a critical role. Some experimental studies show that suppressing the melt flow under strong static magnetic field [7] or microgravity [8]

condition can induce a preferable columnar structure in the castings, further confirming the importance of the crystal transport phenomenon. Another important issue in the formation of as-cast structure is the solidification process subsequent to mold filling. The growth competition between the equiaxed and columnar structures leads to the columnar-to-equiaxed transition (CET) [9]. Similarly, the transport of the equiaxed crystals plays an important role in the event of CET.

In previous studies, the application of the proposed theories to explain the as-cast structure of engineering castings is merely hypothetical, as the quantitative description of the crystal transport phenomenon during mold filling and solidification is difficult. Therefore, the modeling approach becomes a favorable option. Wu et al. have recently used a five-phase volume-average model [10] to calculate the as-cast structure of Al-Cu alloy ingots [11,12]. The nucleation of equiaxed grains, the mixed columnar-equiaxed dendritic solidification, the melt flow and transport of equiaxed crystals, and their influence on the as-cast structure formation have been considered in the model. However, they have ignored the pouring process by assuming the simultaneous filling of the mold at an initial temperature without premature melt solidification. In the current paper, premature melt solidification is refered to the solidification of the melt during mold filling. The model has successfully "reproduced" the as-cast structure of the casting as poured at large superheat, but it has failed to generate the as-cast structure of the casting as poured at low superheat. The assumption of simultaneous mold filling without considering the premature solidification is valid for casting as poured at high superheat, but this assumption is invalid for casting as poured at low superheat. Therefore, the premature solidification during pouring at high superheat is negligible, whereas that during pouring at low superheat is significant. The goal of the current study is to use another numerical tool [13,14] to analyze the influence of the pouring process on the premature solidification. This numerical model considers three phases, namely, air, melt, and equiaxed crystals. The origin of the crystals is assumed to be due to the heterogeneous nucleation in the undercooled melt when it initially contacts with the cold mold during pouring. The transport of the crystals by the melt flow during mold filling, according to the so-called "big bang" theory, is considered. On this basis, the influences of pouring parameters, namely, pouring temperature, initial mold temperature, and pouring rate, on the premature melt solidification and, consequently, on the formation of the as-cast structure can be analyzed.

2 Numerical model and simulation settings

The simulation of the mold filling is conducted using a three-phase globular equiaxed solidification model [13,14]. All conservation equations and closure laws are summarized as follows [15,16]:

1) Mass:

$$\begin{cases} \dfrac{\partial}{\partial t}(f_\ell\rho_\ell)+\nabla\cdot\left(f_\ell\rho_\ell\vec{u}_\ell\right)=-M_{\ell\mathrm{e}} \\ \dfrac{\partial}{\partial t}(f_\mathrm{e}\rho_\mathrm{e})+\nabla\cdot\left(f_\mathrm{e}\rho_\mathrm{e}\vec{u}_\mathrm{e}\right)=M_{\ell\mathrm{e}} \\ \dfrac{\partial}{\partial t}(f_\mathrm{a}\rho_\mathrm{a})+\nabla\cdot\left(f_\mathrm{a}\rho_\mathrm{a}\vec{u}_\mathrm{a}\right)=0 \end{cases}, \tag{1}$$

with $f_\mathrm{a}+f_\ell+f_\mathrm{e}=1$, f_a, f_ℓ, and f_e are volume fractions (dimensionless), ρ_a, ρ_ℓ, and ρ_e are densities (unit: kg/m^3), $\vec{u}_\mathrm{a}$, $\vec{u}_\ell$, and $\vec{u}_\mathrm{e}$ are velocities (unit: m/s), and $M_{\ell\mathrm{e}}$ is mass transfer rate (unit: kg/s/m^3), where subscripts, a, ℓ, and e, indicate air, liquid, and equiaxed phases, respectively.

2) Momentum:

$$\begin{cases} \dfrac{\partial}{\partial t}\left(f_\ell\rho_\ell\vec{u}_\ell\right)+\nabla\cdot\left(f_\ell\rho_\ell\vec{u}_\ell\otimes\vec{u}_\ell\right) \\ =-f_\ell\nabla p+\nabla\cdot\bar{\bar{\tau}}_\ell+f_\ell\rho_\ell\vec{g}-\vec{U}_{\ell\mathrm{e}}-\vec{U}_{\ell\mathrm{a}} \\ \dfrac{\partial}{\partial t}\left(f_\mathrm{e}\rho_\mathrm{e}\vec{u}_\mathrm{e}\right)+\nabla\cdot\left(f_\mathrm{e}\rho_\mathrm{e}\vec{u}_\mathrm{e}\otimes\vec{u}_\mathrm{e}\right) \\ =-f_\mathrm{e}\nabla p+\nabla\cdot\bar{\bar{\tau}}_\mathrm{e}+f_\mathrm{e}\rho_\mathrm{e}\vec{g}+\vec{U}_{\ell\mathrm{e}}-\vec{U}_{\mathrm{ea}} \\ \dfrac{\partial}{\partial t}\left(f_\mathrm{a}\rho_\mathrm{a}\vec{u}_\mathrm{a}\right)+\nabla\cdot\left(f_\mathrm{a}\rho_\mathrm{a}\vec{u}_\mathrm{a}\otimes\vec{u}_\mathrm{a}\right) \\ =-f_\mathrm{a}\nabla p+\nabla\cdot\bar{\bar{\tau}}_\mathrm{a}+f_\mathrm{a}\rho_\mathrm{a}\vec{g}+\vec{U}_{\ell\mathrm{a}}+\vec{U}_{\mathrm{ea}} \end{cases}, \tag{2}$$

where p is pressure, $\bar{\bar{\tau}}_\ell$, $\bar{\bar{\tau}}_\mathrm{e}$, and $\bar{\bar{\tau}}_\mathrm{a}$ are stress tensors (unit: kg/m/s^2), $\vec{U}_{\ell\mathrm{a}}$, $\vec{U}_{\ell\mathrm{e}}$, and $\vec{U}_{\mathrm{ea}}$ are momentum exchange (unit: kg/m^2/s^2), and $\vec{g}$ is the gravity acceleration (unit: m/s^2).

3) Species:

$$\begin{cases} \dfrac{\partial}{\partial t}(f_\ell\rho_\ell c_\ell)+\nabla\cdot\left(f_\ell\rho_\ell\vec{u}_\ell c_\ell\right)=-C_{\ell\mathrm{e}} \\ \dfrac{\partial}{\partial t}(f_\mathrm{e}\rho_\mathrm{e}c_\mathrm{e})+\nabla\cdot\left(f_\mathrm{e}\rho_\mathrm{e}\vec{u}_\mathrm{e}c_\mathrm{e}\right)=C_{\ell\mathrm{e}} \end{cases}, \tag{3}$$

where c_ℓ and c_e are species mass fractions (dimensionless), and $C_{\ell\mathrm{e}}$ is species exchange (unit: kg/m^3/s).

4) Energy:

$$\begin{cases} \dfrac{\partial}{\partial t}(f_\ell\rho_\ell h_\ell)+\nabla\cdot\left(f_\ell\rho_\ell\vec{u}_\ell h_\ell\right)=\nabla\cdot(f_\ell k_\ell\nabla\cdot T_\ell)-Q_{\ell\mathrm{e}}-Q_{\ell\mathrm{a}} \\ \dfrac{\partial}{\partial t}(f_\mathrm{e}\rho_\mathrm{e}h_\mathrm{e})+\nabla\cdot\left(f_\mathrm{e}\rho_\mathrm{e}\vec{u}_\mathrm{e}h_\mathrm{e}\right)=\nabla\cdot(f_\mathrm{e}k_\mathrm{e}\nabla\cdot T_\mathrm{e})+Q_{\ell\mathrm{e}}-Q_{\mathrm{ea}} \\ \dfrac{\partial}{\partial t}(f_\mathrm{a}\rho_\mathrm{a}h_\mathrm{a})+\nabla\cdot\left(f_\mathrm{a}\rho_\mathrm{a}\vec{u}_\mathrm{a}h_\mathrm{a}\right)=\nabla\cdot(f_\mathrm{a}k_\mathrm{a}\nabla\cdot T_\mathrm{a})+Q_{\ell\mathrm{a}}+Q_{\mathrm{ea}} \end{cases}, \tag{4}$$

where $h_\ell=h_\ell^{\mathrm{ref}}+\int_{T_{\mathrm{ref}}}^{T_\ell}c_\mathrm{p}^\ell\mathrm{d}T$, $h_\mathrm{e}=h_\mathrm{e}^{\mathrm{ref}}+\int_{T_{\mathrm{ref}}}^{T_\mathrm{e}}c_\mathrm{p}^\mathrm{e}\mathrm{d}T$, $h_\mathrm{a}=$

$h_a^{ref} + \int_{T_{ref}}^{T_a} c_p^a dT$, the latent heat of fusion (unit: J/kg) $L = h_\ell^{ref} - h_e^{ref}$, h_ℓ, h_e, and h_a are enthalpy (unit: J/kg), h_ℓ^{ref}, h_e^{ref}, and h_a^{ref} are reference enthalpy (unit: J/kg), T_ℓ, T_e, and T_a are temperatures (unit: K), T_ℓ^{ref}, T_e^{ref}, and T_a^{ref} are reference temperatures (unit: K), k_ℓ, k_e, and k_a are thermal conductivities (unit: W/m/K), and c_p^ℓ, c_p^e, and c_p^a is the specific heat (unit: J/kg/K).

5) Grain transport:

$$\frac{\partial}{\partial t} n + \nabla \cdot \left(\vec{u}_e n \right) = \dot{n}, \tag{5}$$

where $\dot{n} = \frac{d(\Delta T)}{dt} \cdot \frac{n_{max}}{\sqrt{2\pi} \cdot \Delta T_\sigma} \cdot e^{-\frac{1}{2}\left(\frac{\Delta T - \Delta T_N}{\Delta T_\sigma}\right)^2}$, $\Delta T = T_f + mc_\ell - T_\ell$, n is the grain number density (unit: m^{-3}), $\dot{n}$ is the nucleation rate (unit: $m^{-3} \cdot s^{-1}$), n_{max} is the maximum grain number density (unit: m^{-3}), ΔT_N is the undercooling at maximum nucleation rate (unit: K), ΔT_σ is the standard deviation of Gaussian distribution (unit: K), ΔT is undercooling (unit: K), T_f is the melting point of solvent (unit: K), and m is the slope of liquidus (unit: K).

6) Mass transfer term:

$$M_{\ell e} = \frac{2D_\ell}{d_e} \frac{c_\ell^* - c_\ell}{c_\ell^*(1-k)} n\pi d_e^2 \rho_e (1 - f_e), \tag{6}$$

where d_e is grain diameter (unit: m) and $d_e = \sqrt[3]{6f_e/n\pi}$, D_ℓ is diffusion coefficient (unit: $m^2 \cdot s^{-1}$), k is solute partition coefficient (dimensionless), and c_ℓ^* is equilibrium concentration.

7) Momentum exchange term:

$$\begin{cases} \vec{U}_{\ell a} = K_{\ell a}\left(\vec{u}_\ell - \vec{u}_a \right) \\ \vec{U}_{ea} = K_{ea}\left(\vec{u}_e - \vec{u}_a \right), \\ \vec{U}_{\ell e} = \vec{U}_{\ell e}^{p} + \vec{U}_{\ell e}^{d} \end{cases} \tag{7}$$

where $\vec{U}_{\ell e}^{p} = \begin{cases} \vec{u}_\ell M_{\ell e} & \text{for solidification} \\ \vec{u}_e M_{\ell e} & \text{for remelting} \end{cases}$, and $\vec{U}_{\ell e}^{d} = K_{\ell e}\left(\vec{u}_\ell - \vec{u}_e \right)$. $K_{\ell a}$ is the momentum exchange coefficient between liquid and air (unit: $kg \cdot m^{-3} \cdot s^{-1}$), according to Schiller and Naumann model [15]; K_{ea} is the momentum exchange rate between solid grain and air (unit: $kg \cdot m^{-3} \cdot s^{-1}$), according to a symmetric model [16]; and $K_{\ell e}$ is the momentum exchange rate between solid grain and liquid (unit: $kg \cdot m^{-3} \cdot s^{-1}$), according to the Wang and Beckermann model [15].

8) Species transfer terms:

$$C_{\ell e} = \begin{cases} k c_\ell^* M_{\ell e} & \text{for solidification} \\ c_e M_{\ell e} & \text{for remelting} \end{cases}. \tag{8}$$

9) Energy exchange terms:

$$\begin{cases} Q_{\ell e} = H_{\ell e}^*(T_\ell - T_e) \\ Q_{\ell a} = H_{\ell a}^*(T_\ell - T_a), \\ Q_{ea} = H_{ea}^*(T_e - T_a) \end{cases} \tag{9}$$

where $H_{\ell e}^* = 10^{11}\ W \cdot m^{-3} \cdot K^{-1}$ is the volume heat exchange coefficient between liquid and equiaxed phases, $H_{\ell a}^* = 6k_\ell f_\ell f_e N_{u_p}/d_a^2$ is the volume heat exchange coefficient between liquid and air, and $H_{ea}^* = h_{ea} f_e f_a$ is the volume heat exchange coefficient between equiaxed and air phases. d_a is the characteristic diameter of air (unit: m), N_{u_p} is the Nusselt number (dimensionless), and h_{ea} is the empirical volume heat exchange coefficient between equiaxed and air phases.

The three phases include the air, liquid melt, and solidifying globular equiaxed crystals, whose volume fractions (velocities) are f_a, f_ℓ, and f_e, respectively. The morphology of the equiaxed crystals is assumed to be spherical. The solidification/remelting-induced mass exchange between the liquid and the solid phases is determined by the diffusion-governed growth kinetics. Latent heat is treated as the enthalpy difference between the liquid and the solid phases. No mass or species exchange occurs between the air and the metal phases, but the energy and momentum exchanges between them are considered.

The nucleation and dissolution of globular equiaxed crystals are assumed to obey the same nucleation law (Eq. (5)) under supercooled and superheated conditions. The nucleation with a positive source term of $\dot{n}$ occurs in an undercooled melt. When the solid-liquid mixture is superheated, remelting occurs, a negative source term is applied to the grain transport equation (Eq. (5)), and a proportion of the previously activated nuclei dissolve. The nucleation parameters for the Al-4.0 wt.% Cu alloy were determined experimentally as follows: $n_{max} = 1.48 \times 10^{11}\ m^{-3}$, $\Delta T_N = 28.84$ K, $\Delta T_\sigma = 10.17$ K [17]. The initial melt is assumed to carry a trace amount of equiaxed crystals with an initial grain number density, a solid fraction, and a crystal diameter of $10^6\ m^{-3}$, 10^{-6}, and 1 μm, respectively. These values are adopted to avoid the absolute zero as the initial transport quantities or parameters. Taking smaller values would not influence the calculation results but instead degrade the numerical convergence efficiency. The dissolution of nuclei and remelting of crystals are limited with such small values. The three-phase model is implemented in an Eulerian multiphase CFD code (ANSYS Fluent 14.x) [16]. Including the air phase requires very fine mesh to account for the distinct liquid/air interface and consequently increases the computational time. A time step of 10^{-5} s is used to initialize the calculation, and it is updated to 10^{-4} s during the later stages of the mold filling.

The reference ingot is calculated using the parameters shown in Fig. 1. The binary alloy with the initial concentra-

tion of Al-4.0 wt.% Cu and an initial temperature of T_p = 973 K is poured from the inlet into a graphite mold. The initial mold temperature, T_m, is 293 K. On the basis of casting experiments, the pouring speed, v_p, is estimated to be 1.04 $m \cdot s^{-1}$ for a corresponding filling time of 5.2 s. A constant heat exchange rate of 120 $W \cdot m^{-2} \cdot K^{-1}$ is maintained on the outer walls of the mold and 2900 $W \cdot m^{-2} \cdot K^{-1}$ at the mold/melt interface during mold filling. The mold is initially filled with air ($f_a = 1.0 - 10^{-6}$) at ambient temperature. During pouring, air escapes from the top of the mold under a pressure outlet boundary condition. Other model parameters and thermal physical properties are available in Ref. [12].

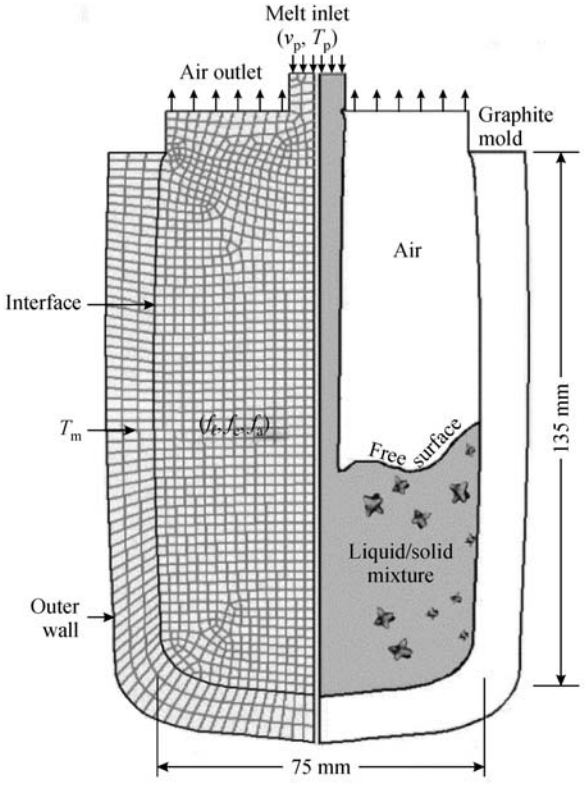

Fig. 1 Geometric configuration of the reference ingot (Al-4.0 wt.% Cu): Grid in the domains of the ingot and mold (left half) and schematic of different phase regions during mold filling (right half) (Both 2D axisymmetric and complete 3D calculations were performed, but the grid is shown here in 2D axis symmetry.)

3 Simulation results

The sequence of the mold filling is shown in Figs. 2 and 3. The pouring temperature is 973 K. Both 2D axisymmetric and complete 3D calculations are performed. The 3D calculation has an advantage over the 2D axisymmetric one in resolving and reproducing a more realistic flow pattern during mold filling. However, analyzing the process details in 3D is difficult. Therefore, the process analysis is performed on the 2D axisymmetric result.

The melt flow with a pouring temperature of 973 K (liquidus temperature, 922.15 K) and a pouring velocity of 1.037 $m \cdot s^{-1}$ is accelerated by gravity until it hits the bottom of the mold. The liquid metal splashes laterally and upward, thereby coming into contact with the bottom wall of the mold. The melt temperature drops as a result of the heat exchange with the mold. Thus, the advanced metal front is considerably undercooled (also called supercooled) (Fig. 2(a)). When the melt is abruptly undercooled at the front, an extreme nucleation rate, $\dot{n} \approx 8 \times 10^{15}$ $m^{-3} \cdot s^{-1}$, is introduced (Fig. 2(c)). Consequently, solidification occurs immediately in the undercooled melt, and a relatively high f_e is achieved (Fig. 2(b)). The formed crystals are carried by the convective flow to the bulk region (away from the mold wall); some of these crystals will survive while a number of the other crystals will be dissolved. The undercooled melt front retains the highest number density of crystals, i.e., $\sim 5 \times 10^{10}$ m^{-3} (Fig. 2(d)). The so-called premature solidification phenomenon is quantified using two values, namely, the number density of crystals, n, and the volume fraction of the crystals, f_e. The process of transporting the initially formed crystals from the mold wall region to the bulk melt region by the flow confirms the "big bang" theory [4].

At the current filling time (0.4 s), the flow vectors indicate that the melt moves mostly forward. However, at the succeeding filling time (0.47 s, Fig. 2(f)), the advancing front of the undercooled melt withdraws along the vertical mold wall due to the gravity, while the incoming stream of the melt with a temperature approximate to the initial superheat is still pushing forward along the bottom mold wall. This leads to the further redistribution and mixing of the already-formed crystals with the superheated liquid. This mode of mixing leads to the dissolution (death) of some crystals, that is, a negative value of $\dot{n}$, as indicated by the color contour in Fig. 2(g). The birth of new crystals by nucleation is shown by gray scale. As a result of the crystal dissolution (death), the maximum f_e and n decreases from the 0.4 s filling time to the 0.47 filling time, as shown in Figs. 2(c) and 2(g).

The above scenario continues dynamically. The melt front in contact with the cold mold wall moves back and forth, inducing the swinging motion of the free surface. The front of the melt always exhibits the lowest temperature, highest nucleation rate, highest crystal number density, and a relatively high solid volume fraction until the filling time 2 s, as shown in Figs. 2(a)–2(p). At 1.00 s, the bottom corner of the ingot has a high temperature, and this corner corresponds to the region with $f_e \approx 0$, whereas the upper bulk region has a relatively low temperature and, consequently, a relatively high f_e, as shown in Figs. 2(i) and (j). The impact of the falling stream from the inlet gradually decreases with increasing melt level in the mold, and the melt front on the free surface becomes calmer. Thus, after 1.00 s, the nucleation can occur near the bottom of the mold, as shown in Figs. 2(k)

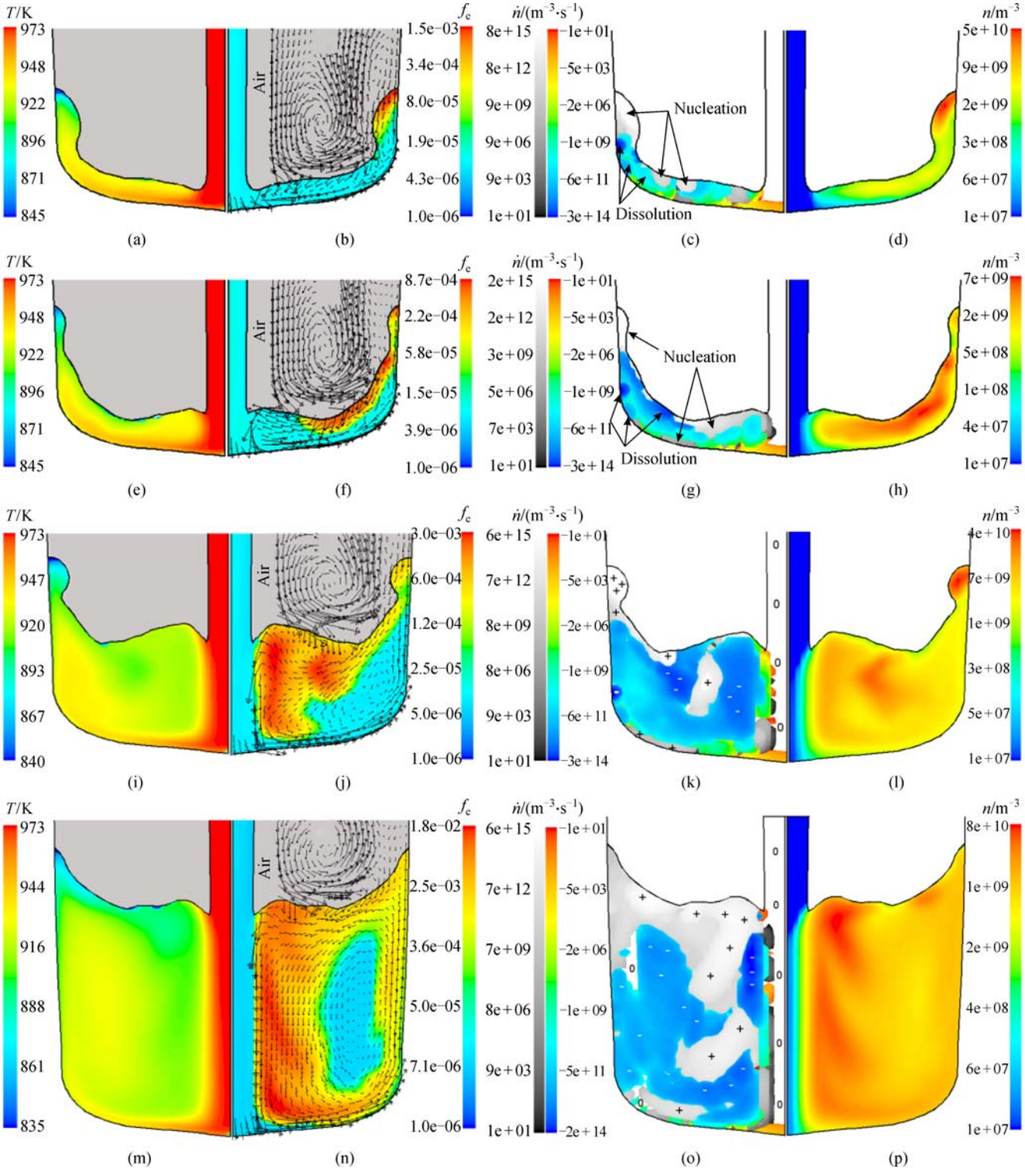
T/K
973
948
922
896
871
845
Air
f_e
1.5e−03
3.4e−04
8.0e−05
1.9e−05
4.3e−06
1.0e−06
(a)
(b)
$\dot{n}$/(m^{-3}·s^{-1})
8e+15
8e+12
9e+09
9e+06
9e+03
1e+01
−1e+01
−5e+03
−2e+06
−1e+09
−6e+11
−3e+14
Nucleation
Dissolution
(c)
n/m^{-3}
5e+10
9e+09
2e+09
3e+08
6e+07
1e+07
(d)
T/K
973
948
922
896
871
845
Air
f_e
8.7e−04
2.2e−04
5.8e−05
1.5e−05
3.9e−06
1.0e−06
(e)
(f)
$\dot{n}$/(m^{-3}·s^{-1})
2e+15
2e+12
3e+09
5e+06
7e+03
1e+01
−1e+01
−5e+03
−2e+06
−1e+09
−6e+11
−3e+14
Nucleation
Dissolution
(g)
n/m^{-3}
7e+09
2e+09
5e+08
1e+08
4e+07
1e+07
(h)
T/K
973
947
920
893
867
840
Air
f_e
3.0e−03
6.0e−04
1.2e−04
2.5e−05
5.0e−06
1.0e−06
(i)
(j)
$\dot{n}$/(m^{-3}·s^{-1})
6e+15
7e+12
8e+09
8e+06
9e+03
1e+01
−1e+01
−5e+03
−2e+06
−1e+09
−6e+11
−3e+14
(k)
n/m^{-3}
4e+10
7e+09
1e+09
3e+08
5e+07
1e+07
(l)
T/K
973
944
916
888
861
835
Air
f_e
1.8e−02
2.5e−03
3.6e−04
5.0e−05
7.1e−06
1.0e−06
(m)
(n)
$\dot{n}$/(m^{-3}·s^{-1})
6e+15
7e+12
7e+09
8e+06
9e+03
1e+01
−1e+01
−5e+03
−2e+06
−1e+09
−5e+11
−2e+14
(o)
n/m^{-3}
8e+10
1e+09
2e+09
4e+08
6e+07
1e+07
(p)

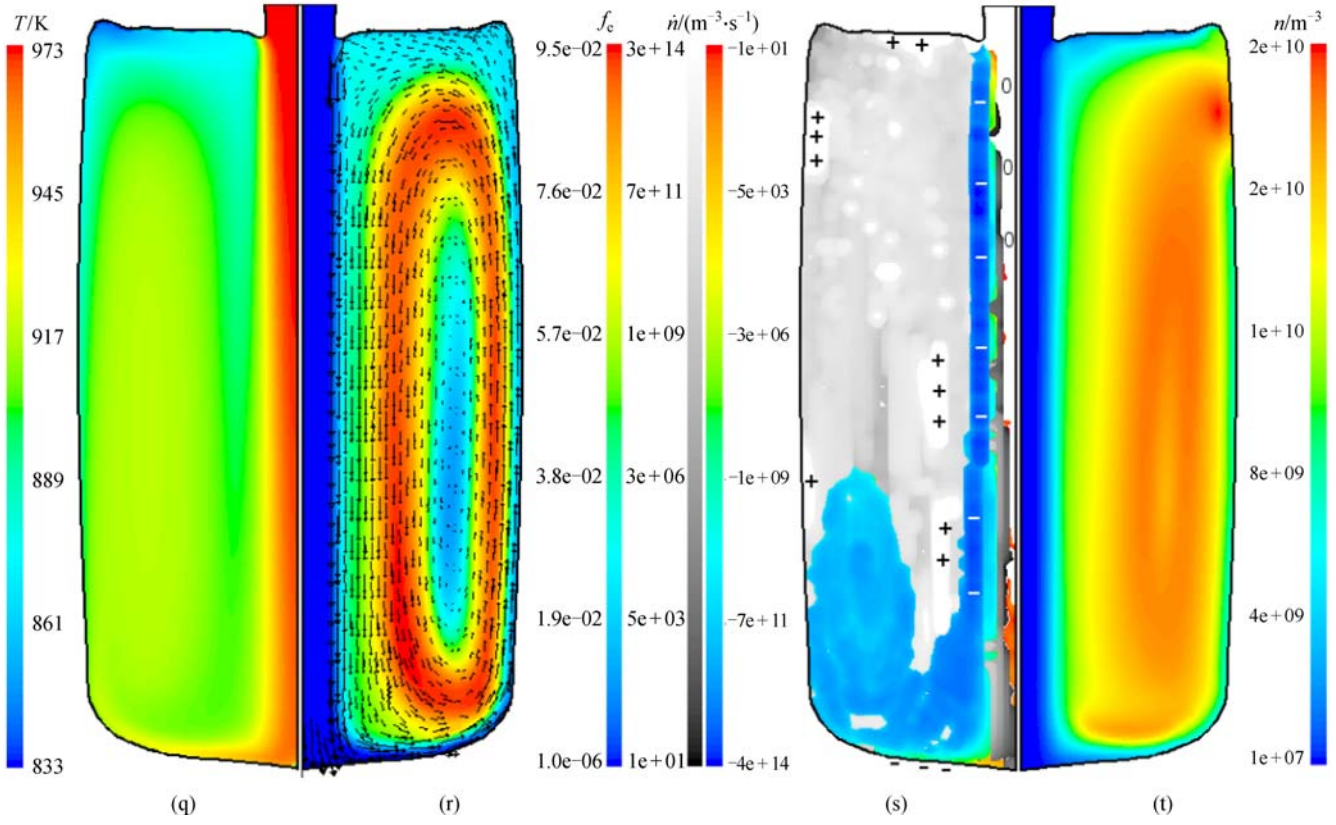

Fig. 2 Contours of (a) T, (b) f_e, (c) $\dot{n}$ in two color scales representing the birth (gray) and death (color) of the nuclei, and (d) n at a filling time of 0.4 s; (e) T, (f) f_e, (g) $\dot{n}$ in color scales representing the birth (gray) and death (color) of the nuclei, and (h) n at a filling time of 0.47 s; (i) T, (j) f_e, (k) $\dot{n}$ in two color scales representing the birth (gray) and death (color) of the nuclei, and (l) n at a filling time of 1.0 s; (m) T, (n) f_e, (o) $\dot{n}$ in two color scales representing the birth (gray) and death (color) of the nuclei, and (p) n at a filling time of 2.0 s; (q) T, (r) f_e, (s) $\dot{n}$ in two color scales representing the birth (gray) and death (color) of the nuclei, and (t) n at a filling time of 5.2 s

and 2(o). The weak flow may engulf a certain amount of crystals from the neighboring region, causing the birth or death of nuclei within the weak falling stream itself, as shown in Figs. 2(k) and 2(s). In general, the swinging motion of the metal surface decays; the region of crystal dissolution expands, spreading over the bottom of the ingot and nearly reaching the superheated zone of the falling stream. During mold filling, the temperature at the top of the ingot is lower than that at the bottom. At the end of the mold filling, the solid crystals are segregated within the flow swirl, as shown in Fig. 2(r). The hot center of the swirl exhibits a very low f_e and n, as shown in Figs. 2(r) and 2(t).

In the real flow pattern, the distributions of T, n, and f_e are highly asymmetric. The fluid dynamics during mold filling is unstable and asymmetric. The 3D calculation results (Fig. 3) are different from those of the 2D axisymmetric results. However, the critical phenomenon captured in the 2D results is also shown in the 3D results. Initially, the superheated melt flow hits the mold bottom, spreading along the mold bottom in all directions, as shown in Figs. 3(a)–3(f). At the melt front, which is in contact with the cold mold, the temperature is always low, a large number of nuclei (as reflected by n) are nucleated, and large amount of crystals (as reflected by f_e) are developed. The melt front position is not axisymmetric, and the T field is highly nonuniform along the peripheral direction. Therefore, the n and f_e distributions are asymmetric. As shown in Figs. 3(d)–3(i), the melt flow carries the n and f_e from the cold melt front to the bulk region, where mixing with the bulk melt as well as the remelting and dissolution of the crystals occur. Although the predicted distributions of n and f_e (Fig. 3(j)–3(l)) in an arbitrary vertical section are different from the 2D axisymmetric results (Fig. 2(q)–2(t)), both 2D and 3D calculations predict that similar amounts of n and f_e survive at the end of the mold filling. In addition, the evolutionary trends of the volume-weighted averages of n and f_e behave similarly between the 2D and 3D calculations, as discussed subsequently. The simulation time for the 3D calculation (average cell size, ~2.13 mm) by using four parallel cores (Intel^{TM} Nehalem 2.93 GHz Cluster) is approximately 8 days. By contrast, the calculation time for the 2D grid (average cell size −2.3 mm) is only 12 h when only one core of the same computing machine. Therefore, the 2D axisymmetric grid is employed in the subsequent analyses.

The volume-weighted averages of quantities T, n, and f_e

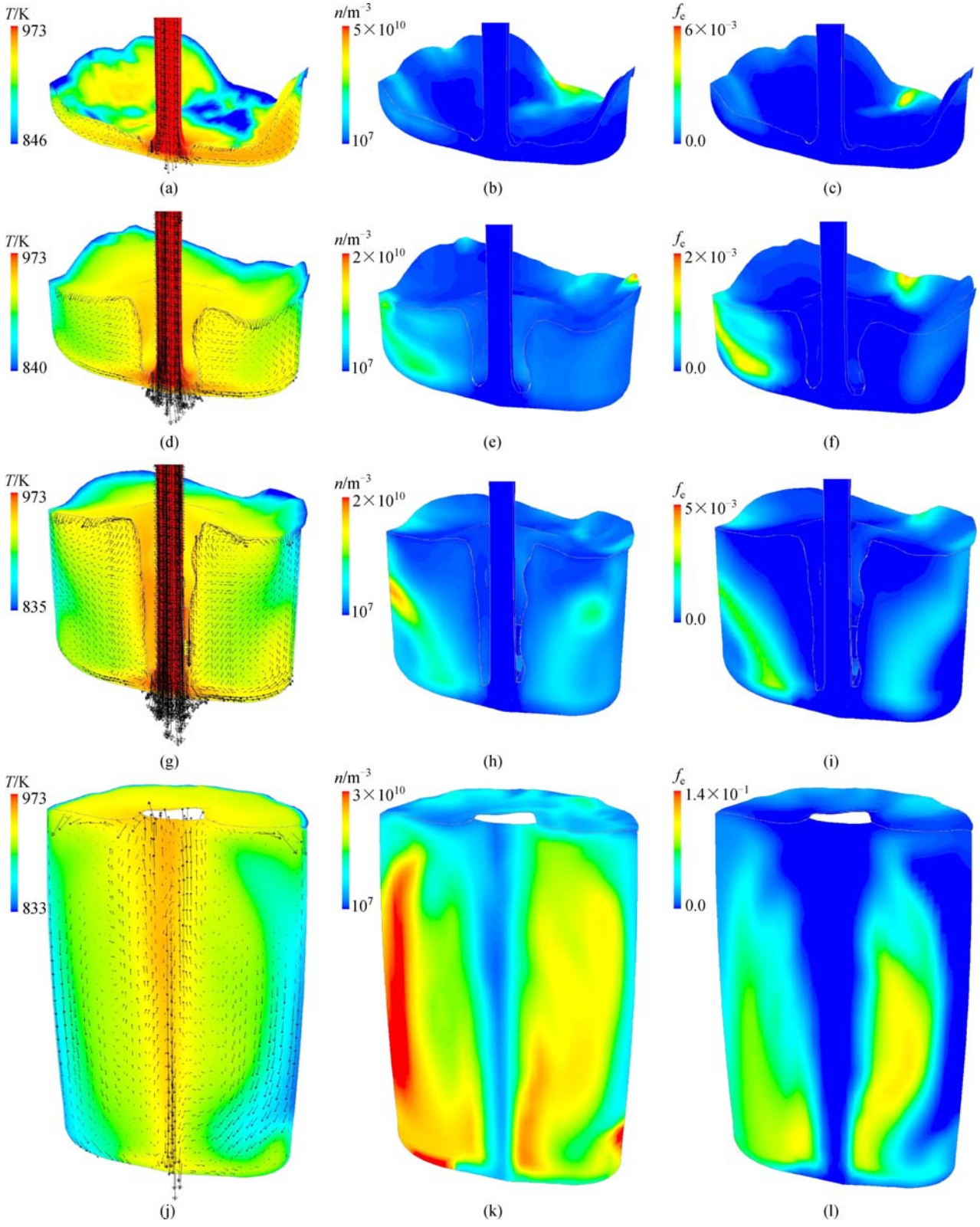

Fig. 3 Contours of (a) T overlaid with $\vec{u}_\ell$, (b) n, and (c) f_e at filling times of 0.4 s; (d) T overlaid with $\vec{u}_\ell$, (e) n, and (f) f_e at filling times of 1.0 s; (g) T overlaid with $\vec{u}_\ell$, (h) n, and (i) f_e at filling times of 2.0 s; (j) T overlaid with $\vec{u}_\ell$, (k) n, and (l) f_e at filling times of 5.24 s (The pouring temperature is 973 K. Only half of the calculation domain is shown. The $\vec{u}_\ell$ vectors are shown in the vertical section.)

as functions of time are plotted in Fig. 4. The average quantity is calculated by $\varphi = (1/V)\sum_{i=1}^{n} \varphi_i |V_i|$ where V is the integral of the metal-filled volume and φ_i and V_i are the monitored quantity and metal-filled volume of element , respectively. The falling melt flow retains its initial pouring temperature until it hits the bottom of the mold at ~0.2 s. At this moment, the melt is abruptly undercooled, and its average temperature drops by more than 40 K. Thereafter, the cooling rate decreases gradually due to the continuous filling of the mold by the superheated melt and heating up of the mold. The thermal behavior of metal is associated with the crystal initiation, which occurs at 0.2 s, when n jumps from an initial value of 10^6 to 7.0×10^9 m^{-3} and f_e reaches ~0.0002. The average n and f_e fluctuate after 0.2 s due to the swinging motion of the melt, as previously explained. The fluctuations decay with time until 1.5 s. The average grain number density gradually increases to the maximum value at ~2.5 s (half-filled mold). The grain number density remains almost constant. However, the crystals continue to grow at a decreasing rate until it reaches a solid fraction of 0.058 at the end of filling. A remarkable feature of the result is shown in Fig. 4, that is, the volume weighted averages of the quantities between 2D and 3D calculations behave similarly. The quantitative difference between the 2D and the 3D may be due to the nature of the asymmetric flow pattern, which cannot be solved in axisymmetric geometry. The grid size (resolution) is also a factor influencing the calculation accuracy, as demonstrated in Section 5.

An advanced five-phase volume average model [10] is used to calculate the as-cast structure of an Al-4.0 wt.% Cu ingot. The as-filled results of the previous mold filling simulation are set as the initial conditions in the calculation of the subsequent mixed columnar-equiaxed solidification by using the five-phase model. The numerical results are compared with the as-cast structures of the ingots poured at different pouring temperatures (Figs. 5 and 6). Very good agreement is achieved. When the ingot is poured at a high temperature (1073 K) with a superheat as high as ~150 K (liquidus temperature, 922.15 K), a mixed columnar-equiaxed structure with distinct equiaxed and columnar zones separated by the columnar-to-equiaxed transition (CET) line, is numerically predicted and experimentally verified. The area of the equiaxed zone enclosed by the CET line (dotted) in Figs. 5 and 6, is similar to the area of the numerically predicted equiaxed zone. The shapes of the CET lines are different between the experimental and numerical results, especially in the upper region. The CET line of the as-cast structure is estimated. Identifying the pure equiaxed zone from the mixed columnar-equiaxed zone on the basis of the metallographic analysis is difficult. The number density at the center of the equiaxed zone reaches ~9×10^8 m^{-3}, which corresponds to a grain size of 1.28 mm. When the ingot is poured at a low temperature (973 K) with a superheat of ~50 K, an early completely equiaxed structure is obtained (Fig. 6). The numerical result shows that a number of small areas exist in the columnar zone in the upper edge and bottom corner; however, these areas are undetectable in the metallographic image. The grains at the center of the equiaxed zone are very fine. The number density reaches 6×10^{10} m^{-3}, which corresponds to a grain size of 320 μm.

The cause of the structural difference between the ingots poured at different pouring temperatures is due to the premature solidification during mold filling. The influences of the pouring parameters on the premature solidification are investigated in the next section.

4 Parametric study

A series of numerical calculations are conducted by varying the pouring parameters T_p, T_m, and v_p, as listed in Table 1, to investigate the influence of the pouring process on the premature solidification of the melt during mold filling. The volume weighted averages of the quantities as functions of filling time are analyzed.

The influence of pouring temperature on the premature solidification is summarized in Fig. 7. All cases present

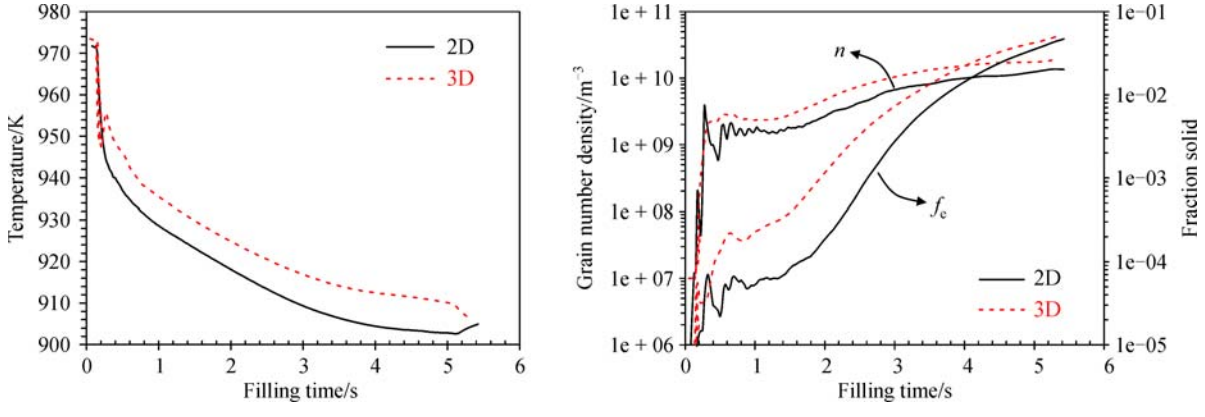

Fig. 4 Average T, n, and f_e as functions of filling time for the ingot poured at 973 K

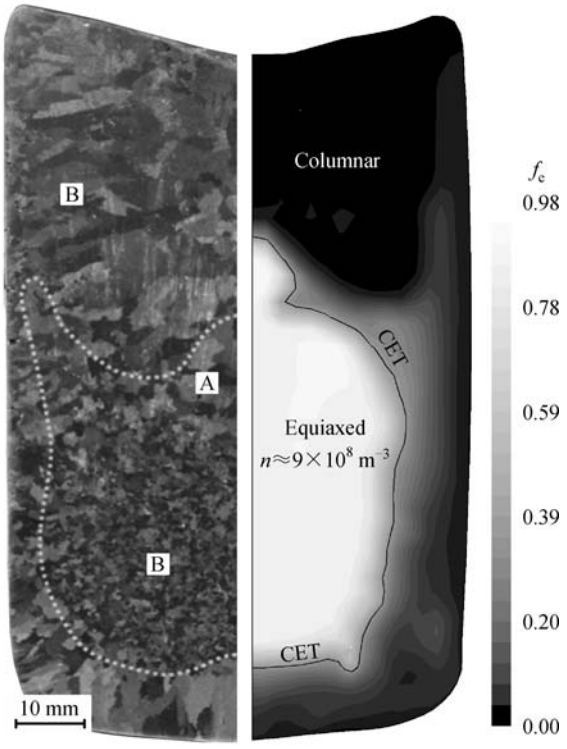

Fig. 5 As-cast structure (left) and the numerically predicted phase distribution (right) in an Al-4.0 wt.% Cu ingot poured at a pouring temperature of 1073 K (The dotted line in the metallographic image presents the estimated columnar-to-equiaxed transition (CET) line.)

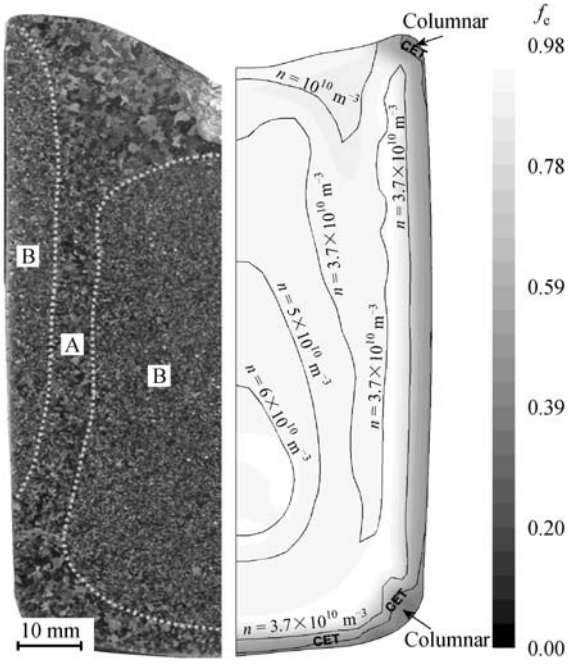

Fig. 6 As-cast structure (left) and the numerically calculated phase distribution (right) in an Al-4.0 wt.% Cu ingot poured at a pouring temperature of 973 K (The dotted lines in the metallographic image separate regions of different grain sizes. The simulation result shows the volume fraction of the equiaxed phase overlaid with isolines of the number density of equiaxed grains.)

similar variation trends of the average melt temperature during filling (Fig. 7(a)). The falling melt retains its pouring temperature until it hits the bottom of the mold at ~0.2 s, after which cooling of the melt starts. Consequently, the mold starts to heat up. The highest cooling rate of the melt occurs immediately after the first falling melt contacts with the bottom mold; thereafter, the cooling rate decreases with time. At the end of the mold filling (5.2 s), large temperature differences among the cases occur. The average temperatures when the pouring temperatures are 1073 K and 1023 K are higher than the liquidus temperature (922.15 K), whereas the average temperatures when the pouring temperatures are 973 K and 963 K are lower than the liquidus temperature.

The cooling process of the melt affects the nucleation and the premature melt solidification, as shown in Figs. 7(b) and 7(c), respectively. Independent of T_p, the nucleation immediately starts when the first melt contacts with the bottom mold (0.2 s). However, the nucleation intensity decreases with T_p. Interestingly, the average n and f_e exhibit fluctuations at the initial stage of the mold filling. This result is mainly due to the immediate nucleation and solidification (release of latent heat) in the undercooled melt, as well as the low as-filled volume at the initial stage. After 3 s, when the entire volume of the mold is nearly filled, this fluctuation phenomenon gradually vanishes. The premature melt solidification in the case of T_p = 1073 K is negligible. At the end of the mold filling, the reduction in T_p to 973 K results in n and f_e values of 1.5×10^{10} m^{-3} and 0.058, respectively.

The initial mold temperature, T_m, has a substantial effect on the premature melt solidification (Fig. 8). The nucleation occurs at approximately 0.2 s, and the nucleation intensity decreases as T_m increases. The nucleation rate decreases progressively thereafter, particularly in high T_m cases. Subsequently, n gradually starts to increase earlier at ~0.6 s in the case of T_m = 393 K, but it is delayed until ~3 s in the case of T_m = 575 K. At the end of the mold filling, the highest average n is obtained in the case with the lowest T_m. An average f_e of ~0.06 is obtained when T_m is the room temperature, whereas a negligible premature solidification is predicted in the case of T_m = 573 K.

The influences of pouring velocity on the evolutionary trends of n and f_e are shown in Fig. 9. The changes in n and f_e with time are similar across the four cases of different pouring rates. The main difference is the duration of the mold filling. The filling time is longer when the pouring velocity is lower. The differences in the grain number densities, n, among the four different pouring rates are not

Table 1 Case definitions of the pouring parameters

Pouring temperature, T_p/K	Initial mold temperature, T_m/K	Cases corresponding to varied pouring velocities (v_p/(m·s^{-1}))			
		0.800	1.037	1.200	1.400
963	293	–	*	–	–
973	293	*	* x	*	*
	423	–	*	–	–
	573	–	*	–	–
1023	293	–	* x	–	–
1073	293	–	* x	–	–

*: Studied numerically; x: Verified experimentally

significant at the end of the mold filling, and their range is 1.2×10^{10}–2.0×10^{10} m^{-3}. However, the premature solidification of the equiaxed phase depends significantly on the pouring velocity: $f_e \approx 0.023$ for $v_p = 1.4$ m·s^{-1}; $f_e \approx 0.1$ for $v_p = 0.8$ m·s^{-1}. Under the same conditions of T_p and T_m, slow pouring provides the activated equiaxed nuclei in the melt with a longer time to grow during the mold filling process; consequently, the equiaxed phase increases.

5 Discussion

The NH_4Cl-H_2O experiment of Jackson et al. [5] provided a method for observing premature melt solidification and crystal motion during filling. In other laboratory experiments, postmortem analyses have been mainly conducted for the study of the as-cast structure castings or ingots [1–9] to figure out the dependency of the as-cast structure on the pouring methods and parameters. Abstracted information from such experiments can only be used to verify the importance of the premature solidification in the subsequent solidification and formation of the final as-cast structure. The information of premature solidification, i.e., n and f_e, during mold filling is impossible to monitor, and its role in the formation of the final as-cast structure is impossible to quantify. The subsequent solidification process, including the mixed columnar-equiaxed crystal growth, thermo-solutal convection, and crystal sedimentation, is also essential to the as-cast structure. Currently, establishing a mathematical model including these contributing events during both mold filling and subsequent solidification can be considered ambitious, but we firmly believe that a complete understanding of the as-cast structure and its dependency on mold filling can only be achieved by using such a model.

Thus, a three-phase model is used to monitor the mold filling sequence with the necessary transport quantities (i.e., T, n, c_ℓ, and f_e) related to the premature melt solidification and the interplay among these quantities. As shown in Fig. 2, the following critical steps of the premature melt solidification process can be tracked as

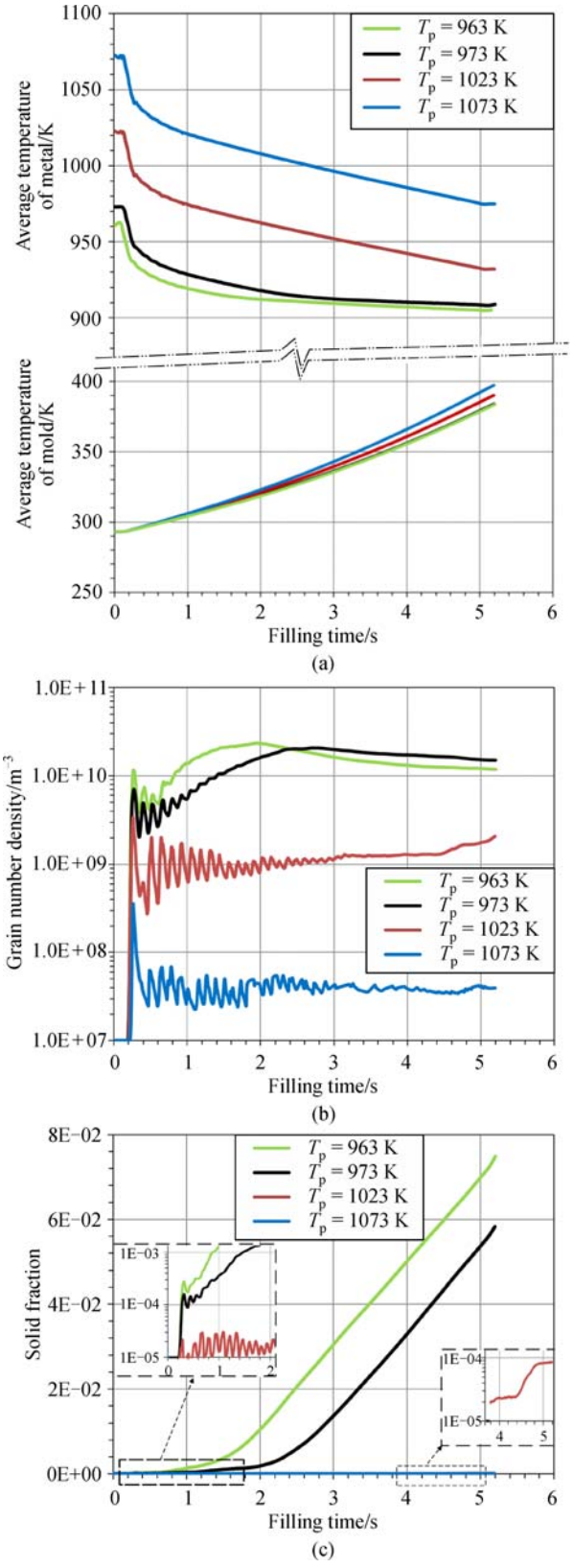

Fig. 7 Influences of pouring temperature on (a) the average temperature of the liquid metal and mold, (b) the number density of crystals, and (c) the volume fraction of solid (T_m = 293 K; v_p = 1.037 m·s^{-1})

follows: The mold filling sequence by considering the melt free surface, the dynamic cooling of the melt due to contact with the cold mold and the reheating due to the flow and mixing with other superheated melt, the onset of the crystal nuclei by the mechanism of heterogeneous nucleation in the undercooled melt, the transport of crystals by the melt flow (big bang theory), the diffusion-governed crystal growth, and the dispersion of crystals and mixing with the superheated melt leading to remelting and dissolution of crystals. The dynamics of the mold filling and premature melt solidification are highly complex. The first melt that hits the bottom of the mold is immediately undercooled; as a result, a high nucleation rate is generated at the melt front. Subsequently, nucleus growth and solidification commence. The melt continuously carries the nuclei (n) and solid crystals (f_e) to the bulk melt region; consequently, both are mixed with the superheated melt, and a proportion of the crystals are remelted and dissolved. The surviving crystals are redistributed in the bulk region following the pattern of the flow. The swinging motion of the free surface near the melt front causes fluctuations in n and f_e. A certain amount of n and f_e remains at the end of the mold filling depending on the pouring conditions (i.e., T_p, T_m, and v_p). The remaining n and f_e, together with the remaining superheat, significantly influences the subsequent solidification. For example, for the ingot poured at $T_p = 1073$ K ($T_m = 293$ K; $v_p = 1.04$ m·s^{-1}), the role of premature solidification is negligible: The average n is in the magnitude of 10^7 m^{-3}, the average f_e is approximately 10^{-4}, and the average temperature of the melt remains higher than the liquidus temperature (Fig. 7). Accordingly, a mixed columnar-equiaxed as-cast structure is obtained, and most equiaxed crystals in this ingot are nucleated during the subsequent solidification process after mold filling (Fig. 5). In another case, the ingot poured at $T_p = 973$ K ($T_m = 293$ K; $v_p = 1.04$ m·s^{-1}) demonstrates significant premature solidification: The average n is in the magnitude of 10^{10} m^{-3}, the average f_e is approximately 0.06, and the average temperature of the melt becomes even slightly below the liquidus temperature (Fig. 7). Therefore, an almost completely equiaxed structure is obtained (Fig. 6). The current modeling example demonstrates that, by considering the premature melt solidification, the as-cast structure can be well "reproduced" numerically. Our recent work has failed to model the as-cast structure of an ingot that was poured at a low temperature [11], because the important role of the premature solidification during mold filing was ignored.

The key premature solidification quantities, which dominantly influence the subsequent solidification and as-cast structure, are the remaining n and f_e at the end of filling. With this point in mind, a parametric study is performed to investigate the influences of the pouring parameters (i.e., T_p, T_m, and v_p) on the remaining n and f_e. The higher the T_p, the less the remaining n and f_e (Fig. 7). Similarly, the higher the T_m, the less the remaining n and f_e (Fig. 8). Scholars have successfully used the method of controlling T_p and T_m in modifying the as-cast structure [7,11]. Pouring speed (v_p) has also been considered as an influencing parameter on the premature solidification in existing studies, but the current parametric study shows that the influence of this quantity is weak compared with those of T_p and T_m (Fig. 9).

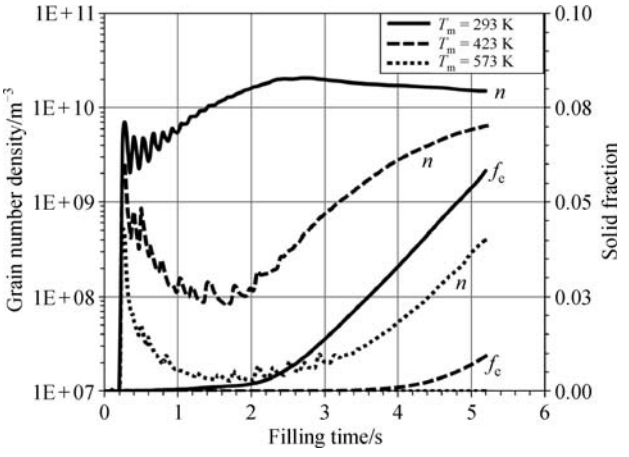

Fig. 8 Influences of the initial mold temperature on average n and f_e (T_p = 973 K; v_p = 1.037 m/s)

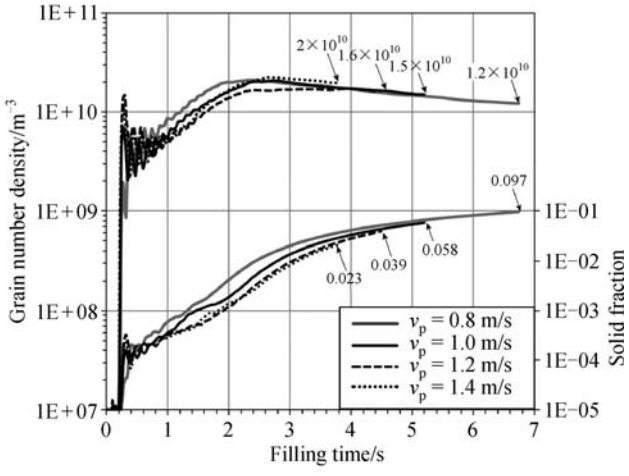

Fig. 9 Influences of pouring velocity on the average grain number density and volume fraction of solid (T_p = 973 K; T_m = 293 K)

At this point, the remaining questions are the uncertainties of the numerical model and the calculation accuracy. The agreement between the numerical simulation and experimental results, which is presented in Figs. 5 and 6, supports the numerical model, but further evaluation is desired. Some phenomena during mold filling have to be simplified or disregarded in the numerical model, such as the turbulence of the flow, formation of the oxidation film

(a typical case for an aluminum melt) at the free surface, and dendritic morphology of crystals. For the further verification of the effectiveness of the current model in quantitatively demonstrating the premature solidification during mold filling, an experiment similar to that conducted by Jackson et al. [5] is recommended. In this experiment, the flow field, the development of the crystal number density, and the average crystal size should be further examined.

An important numerical factor influencing the calculation accuracy of the fluid flow is the grid size. Mesh dependency is a general issue in computational fluid dynamics. However, with the capacity of current computer hardware, obtaining grid-convergent modeling results is not feasible. Therefore, a study of grid and dimension sensitivity is performed in this study to understand the influence of such a factor. The results are listed in Table 2. A reference case with the following fixed pouring parameters is considered: $T_p = 973$ K; $T_m = 293$ K; $v_p = 1.04$ m/s. The average n and f_e plotted as functions of filling time are compared using cases of different grid sizes and dimensions (Fig. 10). In general, the calculated results of all the grids behave similarly to those presented in the previous sections. Nucleation starts at 0.2 s in all cases. The grain number density reaches a local peak value and subsequently exhibits fluctuations, which decay gradually with time. At the initial stage, the curves of n are different for different grids and dimensions. However, at the end of filling (5.2 s), similar n values are obtained for all grids. The evolution of f_e is more sensitive to the grid size. The curves of f_e for grid sizes of 1.2 and 0.67 mm are more similar with each other compared with the curve for a grid size of 2.3. However, we still cannot obtain grid-convergent results. The difference between the curves obtained by 2D axisymmetric calculation (grid size 2.3 mm) and complete 3D calculation (grid size 2.13 mm) are similar.

Table 2 Case definitions for the grid sensitivity study

Calculated type	Number of volume elements	Cell size/mm
2Da	121	2.3
2Db	4500	1.2
2Dc	11000	0.67
3D	85000	2.13

6 Conclusions

This modeling study has confirmed the importance of the premature melt solidification during mold filling in the formation of the final as-cast structure. When the casting is filled at lower superheat, the crystals forming in the melt of the cold region near the mold wall are carried to the bulk melt by the melt flow. This mechanism is in accordance with the "big bang" theory. At the end of the mold filling, these crystals survive the superheat and continue to grow in competition with the columnar structure grown in the outer wall region. As a result, a mixed columnar-equiaxed or even a dominant equiaxed structure is developed. This modeling result is in consistent with the laboratory experimental result. Therefore, the numerical models that ignore the premature melt solidification during mold filling could generate errors in the estimation of the as-cast structure. The three-phase mold filling model, which considers the globular equiaxed solidification, is used in this study. It provides an effective tool for analyzing the premature melt solidification. Further model evaluation is desired.

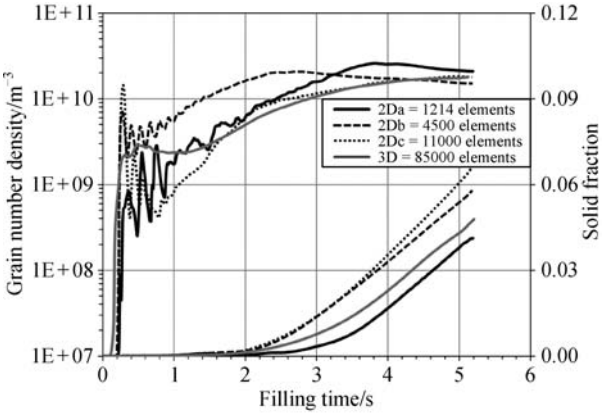

Fig. 10 Comparison of the calculated average n and f_e for various 2D grid sizes and 3D

Acknowledgements This work was financially supported by the FWF Austrian Science Fund (Grant No. P23155-N24), the Austrian Research Promotion Agency (FFG) through the Bridge Early Stage project (Grant No. 842441), the Austrian Federal Ministry of Economy, Family and Youth, and the National Foundation for Research, Technology and Development.

References

1. Spittle J, Dellamore G, Smith R. Formation of equiaxed zone in small ingots. In: Proceedings of the Conference on the Solidification of Metals. Brighton, 1967, 318–322
2. Stefanescu D M. Science and Engineering of Casting Solidification. New York: Kluwer Academic/Plenum Publishers, 2002, 119–126
3. Winegard W, Chalmers B. Supercooling and dendritic freezing in alloys. Transactions of American Society for Metals, 1954, 46: 1214–1223
4. Chalmers B. The structure of ingots. Journal of the Australian Institute of Metals, 1963, 8: 255–263
5. Jackson K, Hunt J, Uhlmann D, et al. On origin of equiaxed zone in castings Transactions of the Metallurgical Society of AIME, 1966, 236: 149–158
6. Southin R T. Nucleation of equiaxed zone in cast metals. Transactions of the Metallurgical Society of AIME, 1967, 239:

220–225
7. Morando R, Biloni H, Cole G S, et al. The development of macrostructure in ingots of increasing size. Metallurgical and Materials Transactions, 1970, 1(5): 1407–1412
8. Parazian J M, Kattamis T Z. Effect of reduced gravity on solidification microstructures CH_4Cl-H_2O alloys. Metallurgical Transactions A, 1980, 11(3): 483–493
9. Hunt J D. Steady state columnar and equiaxed growth of dendrites and eutectic. Materials Science and Engineering, 1984, 65(1): 75–83
10. Wu M, Fjeld A, Ludwig A. Modeling mixed columnar-equiaxed solidification with melt convection and grain sedimentation-Part I: Model description. Computational Materials Science, 2010, 50(1): 32–42
11. Wu M, Nunner G, Ludwig A, et al. Evaluation of a mixed columnar-equiaxed solidification model with laboratory castings. IOP Conference Series: Materials Science and Engineering, 2012, 27 (1): 012018
12. Ahmadein M, Wu M, Li J, et al. Prediction of the as-cast structure of Al-4.0 wt.% Cu ingots. Metallurgical and Materials Transactions A, 2013, 44(6): 2895–2903
13. Wang T, Wu M, Ludwig A, et al. Modelling the thermosolutal convection, shrinkage flow and grain movement of globular equiaxed solidification using a three phase model. International Journal of Cast Metals Research, 18(4): 221–228
14. Wang T, Yao S, Zhang X, et al. Modelling of the thermo-solutal convection, shrinkage flow and grain movement during globular equiaxed solidification in a multi-phase system I. Three-phase flow model. Acta Metallurgica Sinica, 2006, 42(6): 584–590 (in Chinese)
15. Wang C Y, Ahuja S, Beckermann C, et al. Multiparticle interfacial drag in equiaxed solidification. Metallurgical and Materials Transactions B, 1995, 26(1): 111–119
16. ANSYS, Inc. ANSYS FLUENT 12.0 User's Guide. 2009
17. Ahmadein M, Pustal B, Berger R, et al. Grain nucleation parameters for aluminum alloys experimental determination and model evaluation. Metallurgical and Materials Transactions A, 2009, 40 (3): 646–653